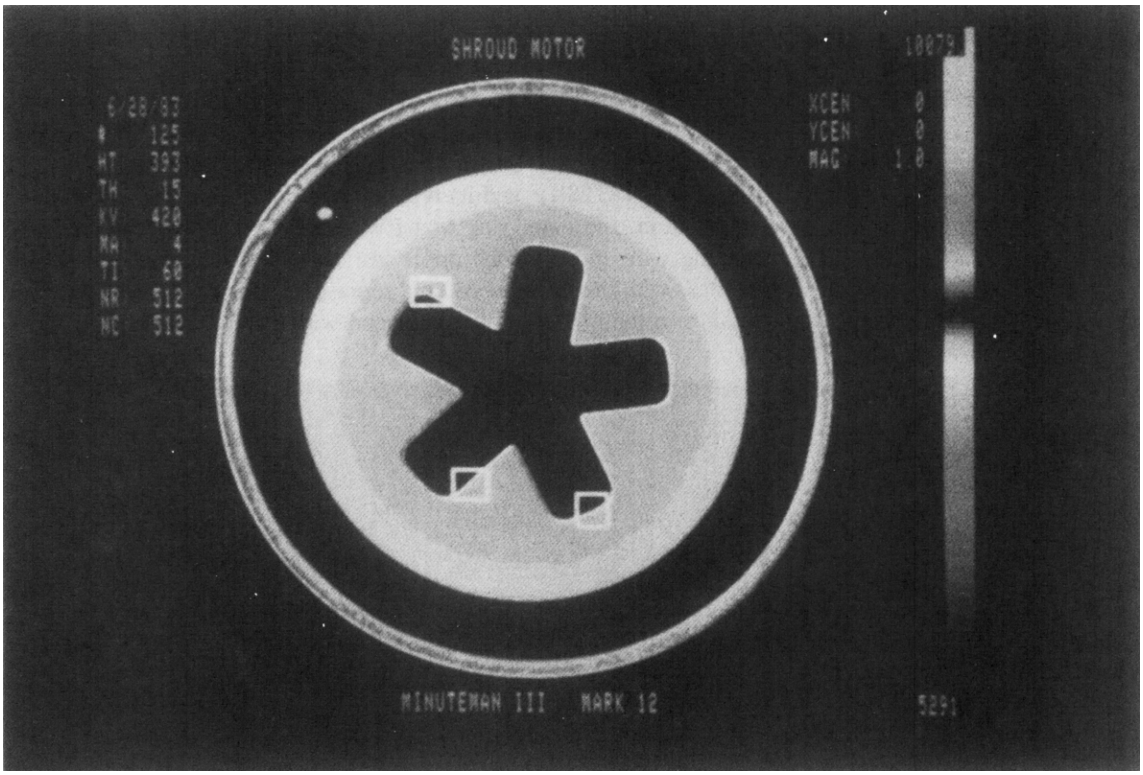

Fig. 4.15: *A cross section of the motor in Fig. 4.14 is shown here. The white squares indicate flaws in the rocket propellant. (Courtesy of Aerojet Strategic Propulsion Company.)*

An Optical Society of America meeting on Industrial Applications of Computerized Tomography described a number of unique applications of CT [OSA85]. These include imaging of core samples from oil wells [Wan85], quality assurance [All85], [Hef85], [Per85], and noninvasive measurement of fluid flow [Sny85] and flame temperature [Uck85].

4.2 Emission Computed Tomography

In conventional x-ray tomography, physicians use the attenuation coefficient of tissue to infer diagnostic information about the patient. Emission CT, on the other hand, uses the decay of radioactive isotopes to image the distribution of the isotope as a function of time. These isotopes may be administered to the patient in the form of radiopharmaceuticals either by injection or by inhalation. Thus, for example, by administering a radioactive isotope by inhalation, emission CT can be used to trace the path of the isotope through the lungs and the rest of the body.

Radioactive isotopes are characterized by the emission of gamma-ray photons or positrons, both products of nuclear decay. (Note that gamma-ray photons are indistinguishable from x-ray photons; different terms are used simply to indicate their origin.) The concentration of such an isotope in any

cross section changes with time due to radioactive decay, flow, and biochemical kinetics within the body. This implies that all the data for one cross-sectional image must be collected in a time interval that is short compared to the time constant associated with the changing concentration. But then this aspect also gives emission CT its greatest potential and utility in diagnostic medicine, because now by analyzing the images taken at different times for the same cross section we can determine the functional state of various organs in a patient's body.

Emission CT is of two types: single photon emission CT and positron emission CT. The word *single* in the former refers to the product of the radioactive decay, a single photon, while in positron emission CT the decay produces a single positron. After traveling a short distance the positron comes to rest and combines with an electron. The annihilation of the emitted positron results in *two* oppositely traveling gamma-ray photons. We will first discuss CT imaging of (single) gamma-ray photon emitters.

4.2.1 Single Photon Emission Tomography

Fig. 4.16 shows a cross section of a body with a distributed source emitting gamma-ray photons. For the purpose of imaging, any very small, nevertheless macroscopic, element of this source may be considered to be an isotropic source of gamma-rays. The number of gamma-ray photons emitted per second by such an element is proportional to the concentration of the source at that point. Assume that the collimator in front of the detector has infinite collimation, which means it accepts only those photons that travel toward it in the parallel ray-bundle R_1R_2. (Infinite collimation, in practice, would imply

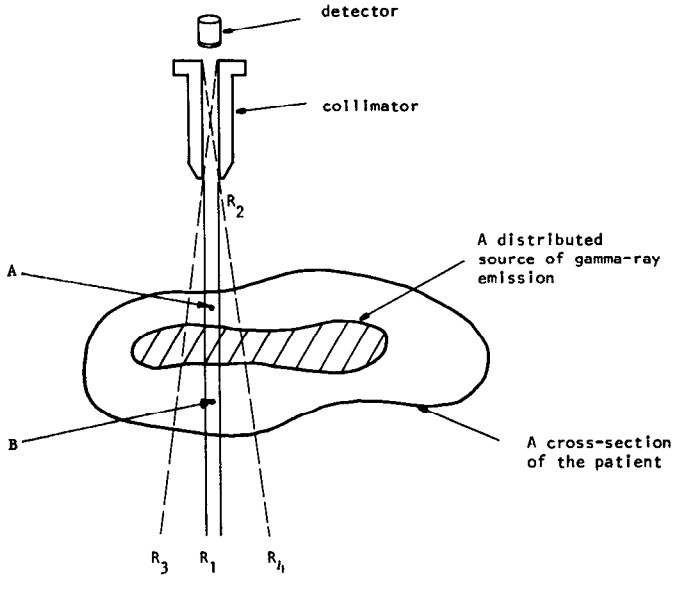

Fig. 4.16: *In single photon emission tomography a distributed source of gamma-rays is imaged using a collimated detector. (From [Kak79].)*

an infinitely long time to make a statistically meaningful observation.) Then clearly the total number of photons recorded by the detector in a "statistically meaningful" time interval is proportional to the total concentration of the emitter along the line defined by R_1R_2. In other words, it is a ray integral as defined in Chapter 3. By moving the detector–collimator assembly to an adjacent position laterally, one may determine this integral for another ray parallel to R_1R_2. After one such scan is completed, generating one projection, one may either rotate the patient or the detector–collimator assembly and generate other projections. Under ideal conditions it should be possible to generate the projection data required for the usual reconstruction algorithms.

Figs. 4.17 and 4.18 show, respectively, axial and sagittal SPECT images of a head. The axial images are normal CT reconstructions at different cross-sectional locations, while the images of Fig. 4.18 were found by reformatting the original reconstructed images into four sagittal views. The reconstructions are 64 × 64 images representing the concentration of an amphetamine tagged with iodine-123. The measured data for these reconstructions consisted of 128 projections (over 360°) each with 64 rays.

As the reader might have noticed already, the images in Figs. 4.17 and 4.18 look blurry compared to the x-ray CT images as exemplified by the reconstructions in Fig. 4.13. To get better resolution in emission CT, one might consider using more detectors to provide finer sampling of each projection; unfortunately, that would mean fewer events per detector and thus a diminished signal-to-noise ratio at each detector. One could consider increasing the dosage of the radioactive isotope to enhance the signal-to-noise ratio, but that is limited by what the body can safely absorb. The length of

Fig. 4.17: *Axial SPECT images showing the concentration of iodine-123 at four cross-sectional planes are shown here. The 64 × 64 reconstructions were made by measuring 128 projections each with 64 rays. (The images were produced on a General Electric 4000T/Star and are courtesy of Grant Gullberg of General Electric in Milwaukee, WI.)*

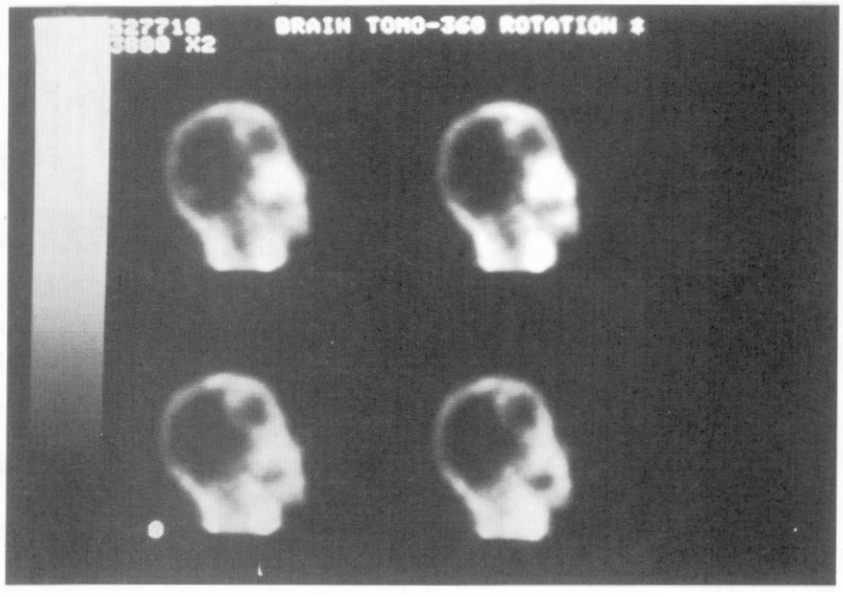

Fig. 4.18: *The reconstructed data in Fig. 4.17 were reformatted to produce the four sagittal images shown here. (The images were produced on a General Electric 4000T/Star and are courtesy of Grant Gullberg of General Electric in Milwaukee, WI.)*

time over which the events are integrated could also be prolonged for an increased signal-to-noise ratio, but usually that is constrained by body motion [Bro81].

A serious difficulty with tomographic imaging of a gamma-ray emitting source is caused by the attenuation that photons suffer during their travel from the emitting nuclei to the detector.[3] The extent of this attenuation depends upon both the photon energy and the nature of the tissue. Consider two elemental sources of equal strength at points A and B in Fig. 4.16: because of attenuation the detector will find the source at A stronger than the one at B. The effect of attenuation is illustrated in Fig. 4.19, which shows reconstructions of a disk phantom for three different values of the attenuation: $\mu = 0.05$, 0.11, and 0.15 cm^{-1}, obtained by using three different media in the phantom. The original disk phantom is also shown for comparison. (These reconstructions were done using 360° of projection data.)

A number of different approaches for attenuation compensation have been developed. These will now be briefly discussed in the following section.

4.2.2 Attenuation Compensation for Single Photon Emission CT

Consider the case where gamma-ray emission is taking place in a medium that can everywhere be characterized by a constant linear attenuation

[3] There is also the difficulty caused by the fact that for a collimator the parallel beam R_1R_2 in Fig. 4.16 is only an idealization. The detector in that figure will accept photons from a point source anywhere within the volume $R_3R_2R_4$. Also, in this volume the response of the detector will decrease as an isotropic source is moved away from it. However, such nonuniformities are not large enough to cause serious distortions in the reconstructions. This was first shown by Budinger [Bud74]. See also [Gus78].

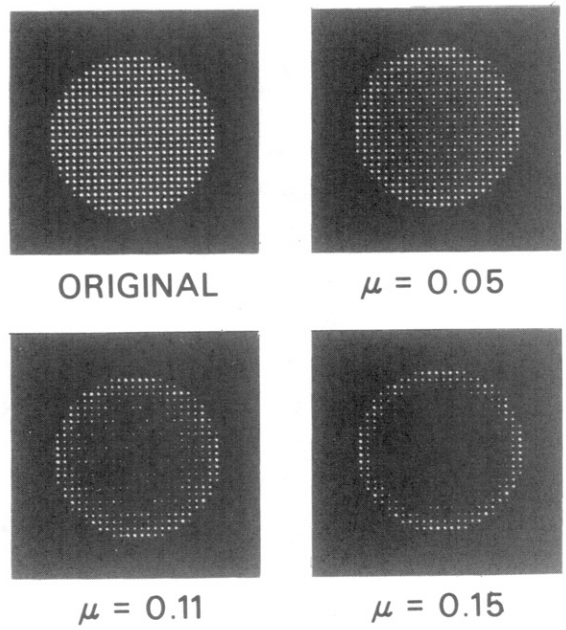

(a)

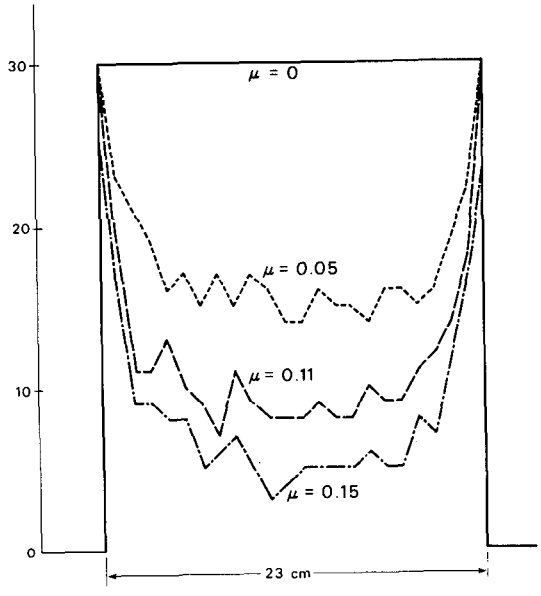

(b)

Fig. 4.19: *Four reconstructions of a gamma-ray emitting disk phantom are shown in (a) for different values of attenuation. (b) shows a quantitative comparison of the reconstructed values on the center line. (Courtesy of T. Budinger.)*

coefficient. Let $\rho(x, y)$ denote the source distribution in a desired cross section. In the absence of any attenuation the projection data $P_\theta(t)$ are given from Chapter 3 by

$$P_\theta(t) = \int\int \rho(x, y)\delta(x \cos\theta + y \sin\theta - t)\, dx\, dy. \tag{24}$$

However, in the presence of attenuation this relationship must be modified to include an exponential attenuation term, $e^{-\mu(d-s)}$, where, as shown in Fig. 4.20, $s = -x \sin\theta + y \cos\theta$ and $d = d(t, \theta)$ is the distance from the line CC' to the edge of the object. Thus the ray integral actually measured is given by

$$P_\theta(t) = \int\int \rho(x, y) \exp[-\mu(d-s)]\delta(x \cos\theta + y \sin\theta - t)\, dx\, dy. \tag{25}$$

For convex objects the distance d, which is a function of x, y, and θ, can be determined from the external shape of the object. We can now write

$$S_\theta(t) = P_\theta(t) \exp[\mu d] = \int\int \rho(x, y) \exp[-\mu(x \sin\theta - y \cos\theta)] \cdot \delta(x \cos\theta + y \sin\theta - t)\, dx\, dy. \tag{26}$$

The function $S_\theta(t)$ has been given the name *exponential Radon transform.* In [Tre80], Tretiak and Metz have shown that

$$\hat{\rho}(r, \phi) = \int_0^{2\pi} \left[\int_{-\infty}^{\infty} S_\theta(r \cos(\theta - \phi) - t)h(t)\, dt \right] \exp[\mu r \sin(\theta - \phi)]\, d\theta \tag{27}$$

is an attenuation compensated reconstruction of $\rho(x, y)$ provided the convolving function $h(t)$ is chosen such that the point spread function of the system given by

$$b(r, \phi) = \int_0^{2\pi} h(r \cos(\theta - \phi)) \exp[\mu r \sin(\theta - \phi)]\, d\theta \tag{28}$$

fits some desired point spread function (ideally a delta function but in practice a low pass filtered version of a delta function). Note that because the integration in (28) is over one period of the integrand (considered as a function of θ), the function $b(r, \phi)$ is independent of ϕ which makes it radially symmetric. Good numerical approximations to $h(t)$ are presented in [Tre80]. In [Tre80] Tretiak and Metz have provided analytical solutions for $h(t)$. Note that (27) possesses a filtered backprojection implementation very similar to that described in Chapter 3. Each modified projection $S_\theta(t)$ is first convolved with the function $h(t)$; the resulting filtered projections are then backprojected as discussed before. For each θ the backprojected contribution at a given pixel is multiplied by the exponential weight $e^{\mu r \sin(\theta - \phi)}$.

Budinger and his associates have done considerable work on incorporating

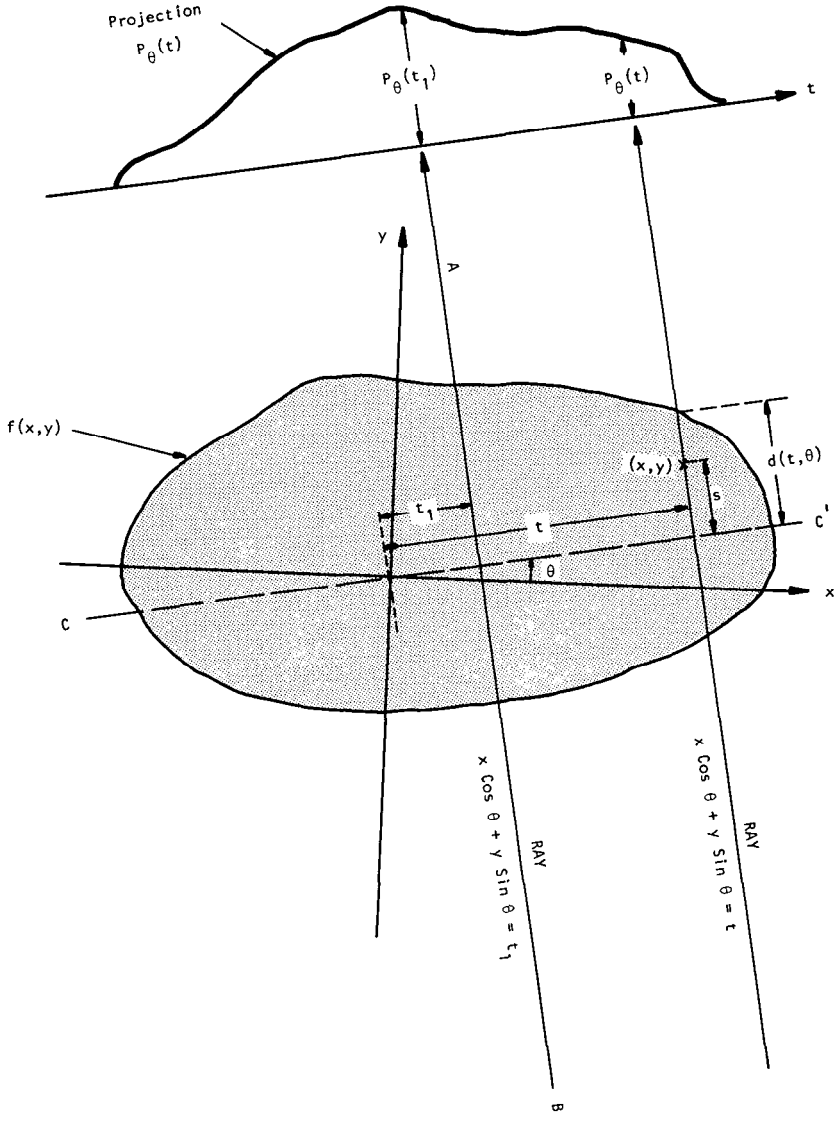

Fig. 4.20: *Several parameters for attenuation correction are shown here. (From [Kak79].)*

attenuation compensation in their iterative least squares reconstruction techniques [Bud76]. In these procedures one approximates an image to be reconstructed by a grid as shown in Fig. 4.21 and an assumption is made that the concentration of the nuclide is constant within each grid block, the concentration in block m being denoted by $\rho(m)$. In the absence of attenuation, the projection measured at a sampling point t_k with projection angle θ_j is given by

$$P_\theta(t_k) = \sum_m \rho(m) f_k^\theta(m) \tag{29}$$

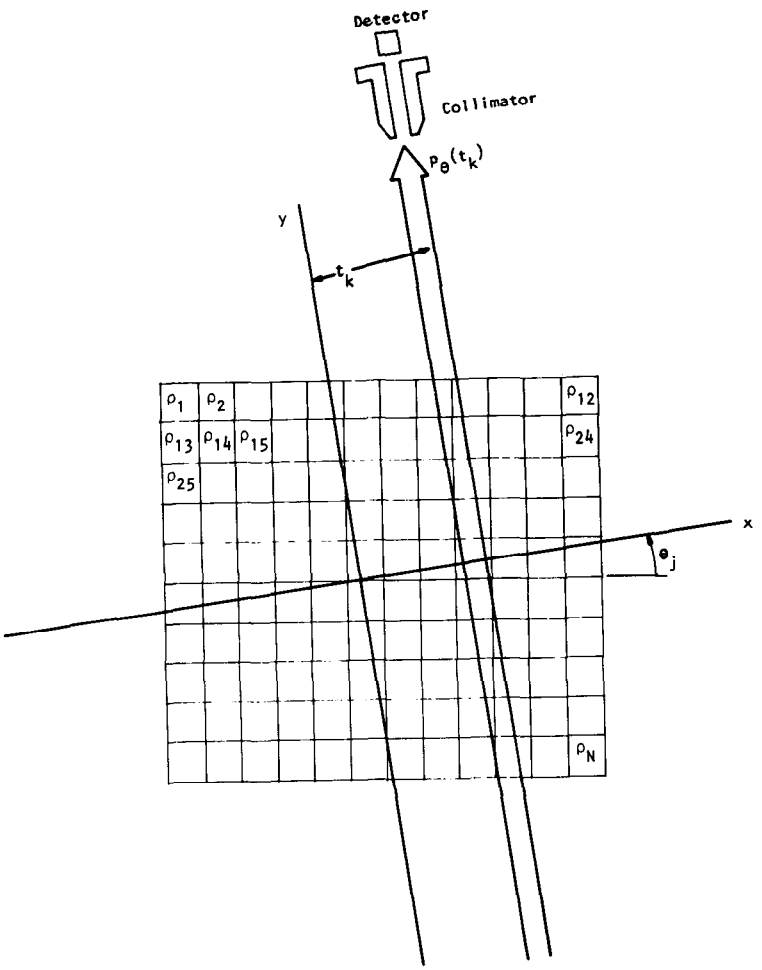

Fig. 4.21: *This figure shows the grid representation for a source distribution. The concentration of the source is assumed to be constant in each grid square. (From [Kak79].)*

where $f_k^\theta(m)$ is a geometrical factor equal to that fraction of the mth block that is intercepted by the kth ray in the view at angle θ. (The above equation may be solved by a variety of iterative techniques [Ben70], [Goi72], [Her71].)

Once the problem of image reconstruction is set up as in (29), one may introduce attenuation compensation by simply modifying the geometrical factors as shown here:

$$P_\theta(t_k) = \sum_{m=1}^{N} \rho(m) f_k^\theta(m) \exp\left[-\mu \ell_m^\theta\right] \tag{30}$$

where ℓ_m^θ is the distance from the center of the mth cell to the edge of the reconstruction domain in the view θ. The above equations could be solved, as any set of simultaneous equations, for the unknowns $\rho(n)$.

Unfortunately, this rationale is flawed: In actual practice the attenuating path length for the mth cell does not extend all the way to the detector or, for that matter, even to the end of the reconstruction domain. For each cell and for a given ray passing that cell it only extends to the end of the object along that ray. To incorporate this knowledge in attenuation compensation, Budinger and Gullberg [Bud76] have used an iterative least squares approach. They first reconstruct the emitter concentration ignoring the attenuation. This reconstruction is used to determine the boundaries of the object by using an edge detection algorithm. With this information the attenuation factors $\exp(-\mu \ell_m^\theta)$ can now be calculated where ℓ_m^θ is now the distance from the mth pixel to the edge of the object along a line $\theta + 90°$. The source concentration is then calculated using the least squares approach. This method, therefore, requires two reconstructions. Also required is a large storage file for the coefficients ℓ_m^θ.

For other approaches to attenuation compensation the reader is referred to [Bel79], [Cha79a], [Cha79b], [Hsi76].

4.2.3 Positron Emission Tomography

With positron emission tomography (PET), we want to determine the concentration and location of a positron emitting compound in a desired cross section of the human body. Perhaps the most remarkable feature of a positron emitter, at least from the standpoint of tomographic imaging, is the fact that an emitted positron can't exist in nature for any length of time. When brought to rest, it interacts with an electron and, as a result, *their masses are annihilated,* creating two photons of 511 keV each. [Note that the mass of an electron (or positron) at rest is equivalent to an energy of approximately 511 keV.] These two photons are called annihilation gamma-ray photons and are emitted at very nearly 180° from one another (Fig. 4.22). It is also important to note that the annihilation of a positron occurs with high probability only after it has been brought to rest. Note that, on the average, 1-MeV and 5-

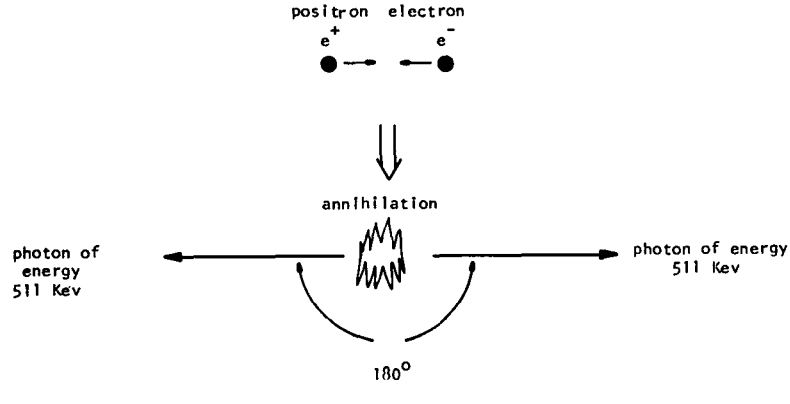

Fig. 4.22: *In positron emission tomography the decay of a positron/electron pair is detected by a pair of photons. Since the photons are released in opposite directions it is possible to determine which ray it came from and measure a projection. (From [Kak79].)*

MeV positrons traverse 4 mm and 2.5 cm, respectively, in water before annihilation. Therefore, for accurate localization it is important that the emitted positrons have as little kinetic energy as possible. Usually, in practice, this desirable property for a positron emitting compound has to be balanced against the competing property that in a nuclear decay if the positron emission process is to dominate over other competing processes, such as electron capture decay, the decay energy must be sufficiently large and, hence, lead to large positron kinetic energy.

The fact that the annihilation of a positron leads to two gamma-ray photons traveling in opposite directions forms the basis of a unique way of detecting positrons. Coincident detection by two physically separated detectors of two gamma-ray photons locates a positron emitting nucleus on a line joining the two detectors. Clearly, a few words about coincident detection are in order. Recall that in emission work, each photon is detected separately and therefore treated as a distinct entity (hence the name "event" for the arrival of a photon). Now suppose the detectors D_1 and D_2 in Fig. 4.23(a) record two photons simultaneously (i.e., in coincidence) that would indicate a positron annihilation on the line joining AA'. We have used the phrase "simultaneous detection" here in spite of the fact that the distances SA and SA' may not be equal. The "coincidence resolving time" of circuits that check for whether the two photons have arrived simultaneously is usually on the order of 10 to 25 ns—a sufficiently long interval of time to make path difference considerations unimportant. This means that if the two annihilation photons arrive at the two detectors within this time interval, they are considered to be in coincidence.

Positron devices have one great advantage over single photon devices discussed in the preceding subsection, that is, electronic collimation. This is

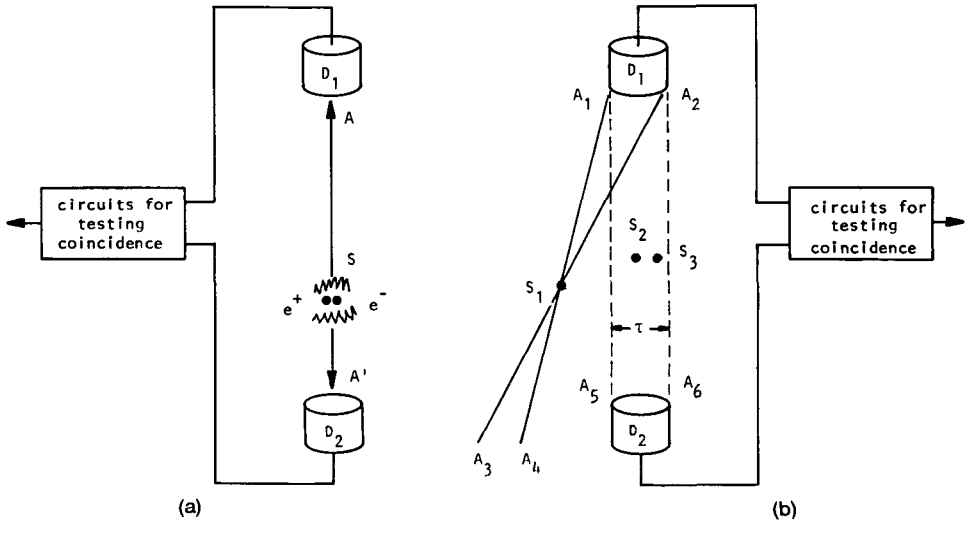

Fig. 4.23: *A pair of detectors and a coincidence testing circuit are used to determine the location of a positron emission. Arrival of coincident photons at the detectors D_1 and D_2 implies that there was a positron emission somewhere on the line AA'. This is known as electronic collimation. (From [Kak79].)*

illustrated by Fig. 4.23(b). Let us say we have a small volume of a positron emitting source at location S_1 in the figure. For all the annihilation photons emitted into the conical volume $A_2S_1A_2$, their counterparts will be emitted into the volume A_3SA_4 so as to miss the detector D_2 completely. Clearly then, with coincident detection, the source S_1 will *not* be detected at all with this detector pair. On the other hand, the source located at S_2 will be detected. Note that, by the same token, if the same small source is located at S_3 it will be detected with a slightly reduced intensity (therefore, sensitivity) because of its off-center location. (This effect contributes to spatial variance of the point spread function of positron devices.) In order to appreciate this electronic collimation the reader should bear in mind that if we had used the detectors D_1 and D_2 as ordinary (meaning noncoincident) gamma-ray detectors (with no collimation), we wouldn't have been able to differentiate between the sources at locations S_1 and S_2 in the figure. The property of electronic collimation discussed here was first pointed out in 1951 by Wrenn *et al.,* [Wre51] who also pointed out how it might be somewhat influenced by background scatter.

It is easy to see how the projection data for positron emission CT might be generated. In Fig. 4.23 if we ignore variations in the useful solid angle subtended at the detectors by various point sources within $A_1A_2A_5A_6$ (and, also, if for a moment we ignore attenuation), then it is clear that the total number of coincident counts by detectors D_1 and D_2 is proportional to the integral of the concentration of the positron emitting compound over the volume $A_1A_2A_5A_6$. This by definition is a ray integral in a projection, provided the width τ shown in the figure is sufficiently small.

This principle has been incorporated in the many positron scanners. As an example, the detector arrangement in the positron system (PETT) developed originally at Washington University by TerPogossian and his associates [Hof76] is shown in Fig. 4.24(a). The system uses six detector banks, containing eight scintillation detectors each. Each detector is operated in coincidence with all the detectors in the opposite bank. For finer sampling of the projection data and also to generate more views, the entire detector gantry is rotated around the patient in 3° increments over an arc of 60°, and for each angular position the gantry is also translated over a distance of 5 cm in 1-cm increments. A multislice version of this scanner is described in [Ter78a] and [Mul78]. These scanners have formed the basis for the development of Ortec ECAT [Phe78]. Many other scanners [Boh78], [Cho76], [Cho77], [Der77b], [Ter78b], [Yam77] use a ring detector system, a schematic of which is shown in Fig. 4.24(b). Derenzo [Der77a] has given a detailed comparison of sodium iodide and bismuth germanate crystals for such ring detector systems. The reader will notice that the detector configuration in a positron ring system is identical to that used in the fixed-detector x-ray CT scanners described in Section 4.1. Therefore, by placing a rotating x-ray source inside the ring in Fig. 4.24(b) one can have a dual-purpose scanner, as proposed by Cho [Cho78]. The reader is also referred to [Car78a] for a characterization of the

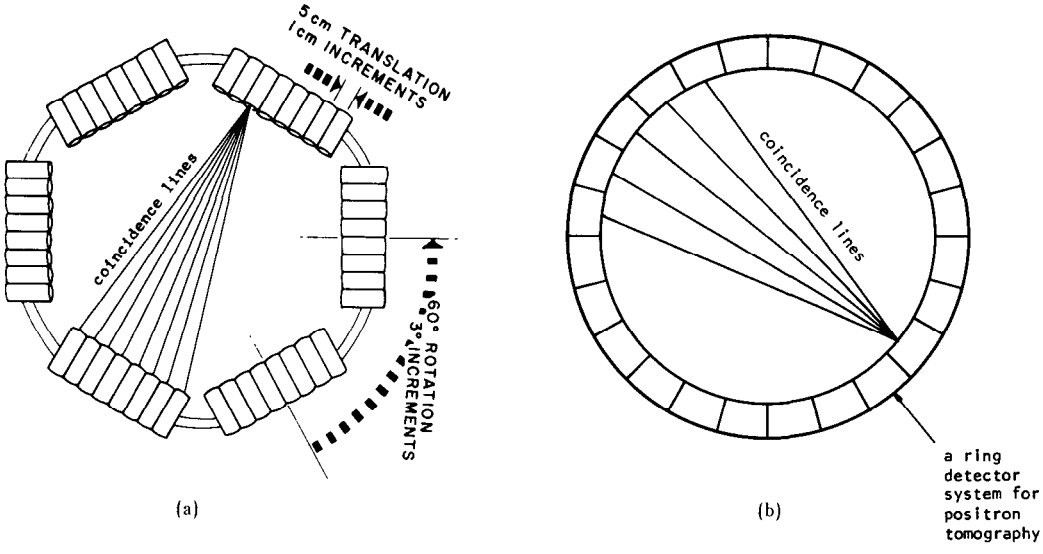

Fig. 4.24: *(a) Detector arrangement in the PETT III CAT. (b) A ring detector system for positron cameras. Each detector in the ring works in coincidence with a number of the other detectors. (From [Kak79].)*

performance of positron imaging systems and to [Bud77] for a comparison of positron tomography with single photon gamma-ray tomography. While our discussion here has focused on reconstructing two-dimensional distributions of positron concentration (from the one-dimensional projection data), by using planar arrays for recording coincidences there have also been attempts at direct reconstruction of the three-dimensional distribution of positrons [Chu77], [Tam78].

4.2.4 Attenuation Compensation for Positron Tomography

Two major engineering advantages of positron tomography over single photon emission tomography are: 1) the electronic collimation already discussed, 2) easier attenuation compensation.[4] We will now show why attenuation compensation is easier in positron tomography.

Let's say that the detectors D_1 and D_2 in Fig. 4.25 are being used to measure one ray in a projection and let's also assume that there is a source of positron emitters located at the point S. Suppose for a particular positron annihilation, the two annihilation gamma-ray photons labeled γ_1 and γ_2 in the figure are released toward D_1 and D_2, respectively. The *probability* of γ_1 reaching detector D_1 is given by

$$\exp\left[-\int_L^{L_1} \mu(x)\, dx\right] \tag{31}$$

[4] On the other hand, one of the disadvantages of positron emission CT in relation to single gamma-ray emission CT is that the dose of radiation delivered to a patient from the administration of a positron emitting compound (radionuclide) includes, in addition to the contribution from the annihilation radiation, that contributed by the kinetic energy of positrons.

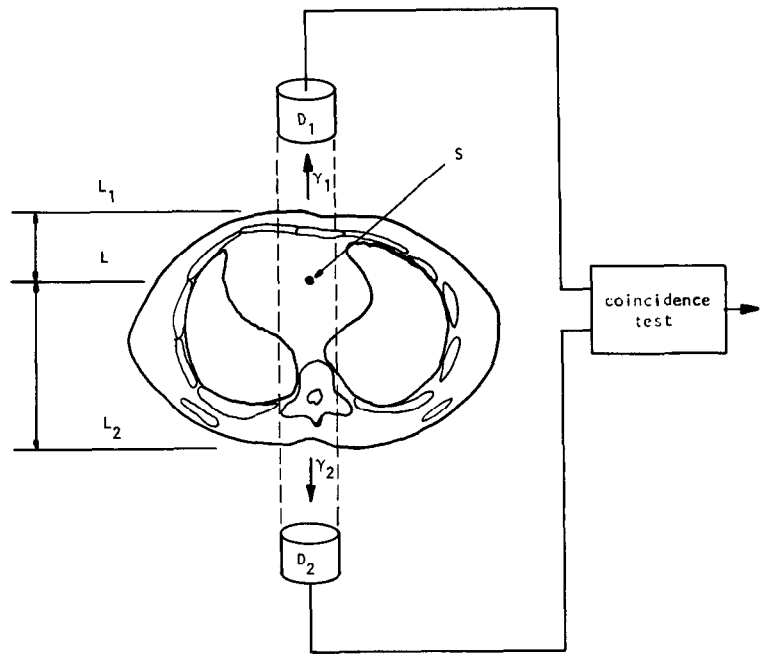

Fig. 4.25: *A photon emitted at S and traveling toward the D_1 detector is attenuated over a distance of $L_1 - L$, while a photon traveling toward the D_2 detector undergoes an attenuation proportional to $L - L_2$. (From [Kak79].)*

where $\mu(x)$ is the attenuation coefficient at 511 keV as a function of distance along the line joining the two detectors. Similarly, the probability of the photon γ_2 reaching the detector D_2 is given by

$$\exp\left[-\int_{L_2}^{L} \mu(x)\, dx\right]. \tag{32}$$

Then the probability that this particular annihilation will be recorded by the detectors is given by the product of the above two probabilities

$$\exp\left[-\int_{L}^{L_1} \mu(x)\, dx\right] \cdot \exp\left[-\int_{L_2}^{L} \mu(x)\, dx\right] \tag{33}$$

which is equal to

$$\exp\left[-\int_{L_2}^{L_1} \mu(x)\, dx\right]. \tag{34}$$

This is a most remarkable result because, first, this attenuation factor is the same no matter where positron annihilation occurs on the line joining D_1 and D_2, and, second, the factor above is exactly the attenuation that a beam of monoenergetic photons at 511 keV would undergo in propagating from L_1 at one side to L_2 at the other. Therefore, one can readily compensate for attenuation by first doing a transmission study (one does not have to do a

reconstruction in this study) to record total transmission loss for each ray in each projection. Then, in the positron emission study, the data for each ray can simply be attenuation compensated when corrected (by division) by this transmission loss factor. This method of attenuation compensation has been used in the PETT and other [Bro78] positron emission scanners.

There are other approaches to attenuation compensation in positron CT [Cho77]. For example, at 511-keV photon energy, a human head may be modeled as possessing constant attenuation (which is approximately equal to that of water). If in a head study the head is surrounded by a water bath, the attenuation factor given by (34) may now be easily calculated from the shape of the water bath [Eri76].

4.3 Ultrasonic Computed Tomography

When diffraction effects can be ignored, ultrasound CT is very similar to x-ray tomography. In both cases a transmitter illuminates the object and a line integral of the attenuation can be estimated by measuring the energy on the far side of the object. Ultrasound differs from x-rays because the propagation speed is much lower and thus it is possible to measure the exact pressure of the wave as a function of time. From the pressure waveform it is possible, for example, to measure not only the attenuation of the pressure field but also the delay in the signal induced by the object. From these two measurements it is possible to estimate the attenuation coefficient and the refractive index of the object. The first such tomograms were made by Greenleaf *et al.* [Gre74], [Gre75], followed by Carson *et al.* [Car76], Jackowatz and Kak [Jak76], and Glover and Sharp [Glo77].

Before we discuss ultrasonic tomography any further it should be borne in mind that the conventional method of using pulse-echo ultrasound to form images is also tomographic—in the sense that it is cross-sectional. In other words, in a conventional pulse-echo B-scan image (see Chapter 8), tissue structures aren't superimposed upon each other. One may, therefore, ask: Why computerized ultrasonic tomography? The answer lies in the fact that with pulse-echo systems we can only see tissue interfaces, although, on account of scattering, there are some returns from within the bulk of the tissue. [Work is now progressing on methods of correlating (quantitatively) these scattered returns with the local properties of tissue [Fla83], [Kuc84]. This correlation is made difficult by the fact that the scattered returns are modified every time they pass through an interface; hence the interest in computed ultrasonic tomography as an alternative strategy for quantitative imaging with sound.]

From the discussion in a previous chapter on algorithms, it is clear that in computerized tomography it is essential to know the path that a ray traverses from the source to the detector. In x-ray and emission tomography these paths are straight lines (within limits of the detector collimators), but this isn't always the case for ultrasound tomography. When an ultrasonic beam